This article has been accepted for publication in a future proceedings of this conference, but has not been fully edited. Content may change prior to final publication.
Citation information: DOI: 10.1109/ICC59461.2026.11587284, ICC 2026 - IEEE International Conference on Communications

Joint Transceiver Beamforming and IRS Phase Shift Design for mmWave MIMO with Modulo ADCs

Yanan Xin
School of Communications and Information Engineering
Chongqing University of Posts and Telecommunications
Chongqing, China
2364679@brunel.ac.uk

Wenyi Yan
Dept. of Engineering
Brunel University of London
London, United Kingdom
Wenyi.Yan@brunel.ac.uk

Lu Gan
Dept. of Engineering
Brunel University of London
London, United Kingdom
Lu.Gan@brunel.ac.uk

Qilie Liu
School of Communications and Information Engineering
Chongqing University of Posts and Telecommunications
Chongqing, China
liuql@cqupt.edu.cn

John Cosmas
Dept. of Engineering
Brunel University of London
London, United Kingdom
John.Cosmas@brunel.ac.uk

***Abstract*—Millimeter-wave (mmWave) multiple-input multiple-output (MIMO) has accelerated the efficiency of modern wireless systems, yet its performance is constrained by the propagation blocking effect and the receiver analog-to-digital converters (ADC) saturation. Motivated by these, this paper first attempted to study an intelligent reflecting surface (IRS)-aided downlink mmWave MIMO system equipped with a modulo ADC front end at the receiver and explicitly models receiver-side quantization error. We propose spectral efficiency (SE) maximization under total-power and constant-modulus constraints and develop a real-valued genetic algorithm-based scheme that, in each generation, (i) explores the IRS reflection matrix and (ii) updates the transceiver beamformers by performing singular value decomposition on the cascaded channel, updated with the IRS reflection matrix. Experimental results demonstrate that the modulo ADC achieves higher SE and lower bit error rates with fewer bit resolution, effectively mitigating saturation-induced clipping and outperforming conventional ADCs.**

***Index Terms*—MmWave, Intelligent reflecting surface, MIMO, Modulo ADC, Beamforming.**

I. Introduction

Millimeter-wave (mmWave) technology promises high capacity and enhanced security [1]. Massive multiple-input multiple-output (MIMO) is a key physical-layer technology for mmWave communications that meets the growing demand for high data rates [2]. However, commercialization remains hampered by blockage, particularly in dense urban environments. To mitigate this, intelligent reflecting surfaces (IRSs), also known as reconfigurable intelligent surfaces (RISs), employ large arrays of passive, reconfigurable elements that impose controlled phase shifts on incident waves. By coherently steering these reflections, IRSs can create virtual line-of-sight links for mmWave systems and, because they require no radio-frequency chains, substantially reduce hardware cost and power consumption compared with active relays [3], [4].

MmWave MIMO combined with IRS is seen as a key path to improve downlink capacity and coverage. The former provides array and multiplexing gain, while the latter reshapes the propagation environment through reflective elements, thus having significant spectrum efficiency (SE) potential within a limited hardware budget [5]. However, translating these gains to real systems is constrained by the power overhead of high-speed, high-resolution analog-to-digital converters (ADCs) and receiver dynamic-range saturation triggered by peaks and rapid fading, which causes clipping and aliasing.

Most existing efforts focus on employing low-resolution ADCs to mitigate power consumption, as discussed in [6]–[11]. Specifically, [6] analyzes IRS-aided mmWave uplink with low-resolution ADCs and oscillator phase noise, deriving achievable-rate expressions and revealing that the rate is fundamentally limited by ADC precision at the base station. [7] studies passive IRS beamforming in a MIMO system with few-bit ADCs at the receiver via a quantization-aware design, combining branch-and-bound search with gradient descent to approach semidefinite relaxation optima and improve rate under stringent bit budgets. [8] analyzes uplink SE for IRS-aided mmWave multiple input single output with low-resolution ADCs, designing IRS phases from statistical

This work is supported in part by Research on Cognitive Non-Orthogonal Multiple Access Communication Based on Intelligent Reflecting Surfaces (D22022024360) under Grant BYJS202318, and in part by the Natural Science Foundation of Chongqing, China, under Grant CSTB2024NSCQ-LZX0134, and in part by the National Natural Science Foundation of China under Grant 62401093.

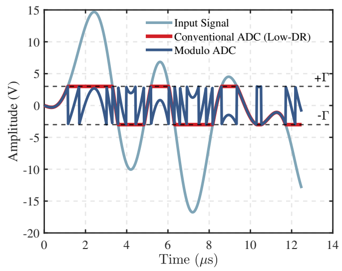

Figure 1. Modulo and conventional ADCs for a 16-QAM input signal. The modulo ADC folds the signal into the range $[-\Gamma, \Gamma)$ without saturation, whereas the conventional ADC clips the output at $\pm\Gamma$.

CSI, deriving a zero-forcing–based SE formula, and Monte-Carlo-verifying SE gains with saturation. [9] addresses reconfigurable intelligent surface-aided hybrid massive MIMO with adaptive-resolution ADCs and proposes a low-complexity decoupling–based alternating maximization with Lagrangian dual transform and fractional programming, achieving robust performance under imperfect cascaded channel state information. [10] performs a wideband RIS-aided massive MIMO-orthogonal frequency-division multiplexing analysis with low-resolution BS ADCs over Rician channels, deriving a closed-form approximated achievable rate and scaling laws that clarify when SE gains are attainable despite coarse quantization. [11] develops joint transmit–receive beamforming and per-chain resolution-adaptive ADC bit allocation under a Bussgang–additive quantization noise model (AQNM) framework, showing SE and energy efficiency gains over fixed-resolution designs. However, the aforementioned works are mostly focused on the low power consumption benefited by the low-resolution feature of the ADC. The effect of low dynamic range (DR) conventional ADC clipping on system gain has not been investigated.

To avoid signal clipping, techniques such as Automatic Gain Control (AGC) adapt to input variations and maintain the baseband signal strength around a target threshold [12], [13]. Modulo ADCs have recently emerged as a promising technology that folds inputs into a bounded dynamic range without saturation, unlike conventional ADCs that clip. The architecture is a hardware–software co-design: hardware performs folding and sampling (Fig. 1), while software algorithms unwrap the folded samples. Recent progress in modulo ADC recovery includes single-channel techniques such as the high-order difference (HoD) method [14], multi-channel strategies based on the robust Chinese Remainder Theorem (RCRT) [15]–[17], and so on. Specifically, [18] proposes a MIMO system with the modulo ADC, which samples to expand the effective dynamic range and avoid saturation, together with a dedicated receiver enabling high-order quadrature amplitude modulation at very low bit resolution. To the best of our knowledge, the impact of ADC clipping on the MIMO system performance metrics, such as spectral efficiency (SE), has not been investigated in the existing literature.

To overcome the aforementioned limitations and explore the factors affecting the SE performance, we make the first attempt to equip the modulo ADC at the receiver front end in an IRS-aided mmWave MIMO system, and design the transceiver beamforming and IRS phase shift jointly. Considering cost and complexity constraints in MIMO systems, this work adopts single-channel modulo ADCs with the HoD method [14], which provides a favorable trade-off between simplicity and performance. The main contributions of this paper are summarized as follows:

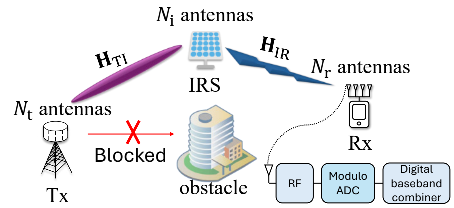

Figure 2. An IRS-aided downlink mmWave MIMO system with Modulo ADC.

- We introduce modulo ADCs into IRS-aided mmWave MIMO downlink systems and propose a real-valued genetic algorithm-based scheme that jointly optimizes the precoder, combiner, and IRS reflection matrix to maximize SE under limited ADC dynamic range and quantization-resolution constraints.
- We investigate the impact of low-resolution ADCs with varying dynamic ranges on system performance, including low dynamic range (DR) with clipping, modulo ADCs, and full DR ADCs.
- Experimental results demonstrate that the modulo ADC attains higher SE and lower BER at lower bit resolutions, effectively suppressing saturation-induced clipping and outperforming conventional ADCs.

II. System Model and Problem Formulation

A. System Model

This work investigates an IRS-aided downlink massive MIMO system with modulo ADC, where the transmitter (Tx) and receiver (Rx) are equipped with N_t and N_r antennas. The direct Tx-Rx link is blocked by an obstacle, and communication is established via an IRS that consists of N_i reflecting elements. The received signal passes through the RF front-end, sampled by the modulo ADCs, and then processed by the digital baseband combiner. As shown in Fig. 2. $\mathbf{s} \in \mathbb{C}^{N_\mathrm{s}}$ denotes the nth transmitted symbol vector, which satisfies $\mathbb{E}[\mathbf{s}\mathbf{s}^\mathrm{H}] = \mathbf{I}_{N_\mathrm{s}}$, where $\mathbf{I}_{N_\mathrm{s}}$ denotes the N_s-dimensional identity matrix. Furthermore, let $\mathbf{F} \in \mathbb{C}^{N_\mathrm{t} \times N_\mathrm{s}}$ be the precoding matrix satisfying the power constraint $\|\mathbf{F}\|_\mathrm{F}^2 \le P_\mathrm{t}$, P_t denotes the transmit power budget of the Tx. The received signal at the Rx without quantization can be written as

$$\mathbf{y} = \mathbf{H}(\mathbf{\Theta})\mathbf{F}\mathbf{s} + \mathbf{n} \in \mathbb{C}^{N_\mathrm{r}} \tag{1}$$

where $\mathbf{n} \sim \mathcal{N}(\mathbf{0}, \sigma^2\mathbf{I})$, σ^2 represents the noise power. $\mathbf{H}(\mathbf{\Theta}) = \mathbf{H}_\mathrm{IR}\mathbf{\Theta}\mathbf{H}_\mathrm{TI} \in \mathbb{C}^{N_\mathrm{r} \times N_\mathrm{t}}$, where $\mathbf{H}_\mathrm{TI} \in \mathbb{C}^{N_\mathrm{i} \times N_\mathrm{t}}$, and $\mathbf{H}_\mathrm{IR} \in \mathbb{C}^{N_\mathrm{r} \times N_\mathrm{i}}$ denote the channel from the transmitter to the IRS and the channel from the IRS to the receiver, respectively. $\mathbf{\Theta} = \mathrm{diag}(\boldsymbol{\theta}) \in \mathbb{C}^{N_\mathrm{i} \times N_\mathrm{i}}$ denotes an IRS diagonal matrix, where $\boldsymbol{\theta} = [\theta_1, \ldots, \theta_{n_\mathrm{i}}, \ldots, \theta_{N_\mathrm{i}}]^\mathrm{H} \in \mathbb{C}^{N_\mathrm{i}\times 1}$ is the reflection vector, $\theta_{n_\mathrm{i}} = \beta e^{j\varphi_{n_\mathrm{i}}}$, $\varphi_{n_\mathrm{i}} \in [0,\ 2\pi)$, $\forall n_\mathrm{i} \in \mathcal{N}_\mathrm{i} = \{1, \ldots, N_\mathrm{i}\}$ denotes the continuous phase shift for the $n_\mathrm{i}^{\mathrm{th}}$ reflecting element, and $\beta \in [0, 1]$ is the amplitude reflection coefficient. We set $\beta = 1$ [19].

The mmWave channel can be modeled using the Saleh-Valenzuela model. The channel matrix is expressed as

$$\mathbf{H}_c = \sum_{l=0}^{L_c-1} a_{c,l}\boldsymbol{\alpha}_r(\phi^r_{c,l}, \varphi^r_{c,l})\boldsymbol{\alpha}_t(\phi^t_{c,l}, \varphi^t_{c,l})^\mathrm{H} \tag{2}$$

where, $c \in \{\mathrm{TI}, \mathrm{IR}\}$, $a_{c,l} = \sqrt{\frac{N_\mathrm{r}N_\mathrm{t}}{L_c}}10^{-\frac{\mathrm{PL}(d_c)}{20}}$ is the complex gain of the $l^{\mathrm{th}}, l \in \{0, ..., L_c - 1\}$ path, $\mathrm{PL}(d_c)$ denotes the pathloss based on distance d_c. Note that $\mathbf{H}_c$ contains both LoS and non-line of sight (NLoS) components. $\boldsymbol{\alpha}_{t(r)}(\phi^{t(r)}_{c,l}, \varphi^{t(r)}_{c,l})$ denotes the normalized transmit and receive array response vectors, where $\phi^t_{c,l}(\varphi^t_{c,l})$ and $\phi^r_{c,l}(\varphi^r_{c,l})$ are the vertical (horizontal) angles of departure and arrival (AoDs, AoAs). Assume that Tx, Rx, and IRS are all deployed with uniform planar arrays (UPA) of size $N_{x,\mathrm{h}} \times N_{x,\mathrm{v}}$ with $N_x = N_{x,\mathrm{h}}N_{x,\mathrm{v}}$, where $x \in \{\mathrm{t}, \mathrm{r}, \mathrm{i}\}$. The array response vector corresponding to the l^{th} path of the Tx/Rx in $\mathbf{H}_c$ is then given by

$$\begin{aligned}&\boldsymbol{\alpha}_{t(r)}(\phi^{t(r)}_{c,l}, \varphi^{t(r)}_{c,l})\\ &= \frac{1}{\sqrt{N_x}}[1, \ldots, e^{j\Delta_x(n_{x,h}\sin(\phi^{t(r)}_{c,l})\sin(\varphi^{t(r)}_{c,l})+n_{x,v}\cos(\varphi^{t(r)}_{c,l}))},\\ &\ldots, e^{j\Delta_x((N_{x,h}-1)\sin(\phi^{t(r)}_{c,l})\sin(\varphi^{t(r)}_{c,l})+(N_{x,v}-1)\cos(\varphi^{t(r)}_{c,l}))}]\end{aligned} \tag{3}$$

where $\Delta_x = \frac{2\pi d_x}{\lambda}$, $d_x = \frac{\lambda}{2}$ denotes the spacing between the Tx/Rx antennas or IRS elements and $\lambda = \frac{c_\mathrm{L}}{f_c}$ denotes the center carrier wavelength, where c_L and f_c denote the speed of light and carrier frequency, respectively. To enhance the system performance, the modulo ADCs are equipped for every antenna on the Rx. We first fold (1), the folded signal can be expressed as [14]

$$\mathbf{r} = \mathcal{M}_\Gamma\{\mathbf{y}\} = \mathbf{y} - 2\Gamma\left\lfloor\frac{\mathbf{y} + \Gamma\mathbf{1}}{2\Gamma}\right\rfloor, \tag{4}$$

where Γ denotes the folding threshold, and $\mathbf{1}$ is the all-ones vector. The recovered signal can then be formulated as

$$\hat{\mathbf{y}} = \mathbf{r} + 2\Gamma\hat{\mathbf{k}}, \tag{5}$$

where $2\Gamma\hat{\mathbf{k}}$ is the recovered residual function which recovered by HoD [14]. To characterize the quantization of (5), we adopt the AQNM [18] on (5). The quantized signal can be expressed as

$$\hat{\mathbf{y}}_\mathrm{q} = \mathcal{Q}_\mathrm{b}(\hat{\mathbf{y}}) \approx \mathbf{A}\hat{\mathbf{y}} + \mathbf{n}_\mathrm{q} \tag{6}$$

where $\mathcal{Q}_\mathrm{b}(\hat{\mathbf{r}})$ denotes perform b-bit uniform quantization on the signal $\hat{\mathbf{y}}$. $\mathbf{A} = \mathrm{diag}(\boldsymbol{\alpha}_\mathrm{q}) \in \mathbb{C}^{N_\mathrm{r}\times N_\mathrm{r}}$, $\boldsymbol{\alpha}_\mathrm{q} = [\alpha_{\mathrm{q},1}, \ldots, \alpha_{\mathrm{q},N_\mathrm{r}}]^\mathrm{T}$ collects the per-ADC gains, with $\alpha_{\mathrm{q},n_\mathrm{r}} = 1 - \rho(b, \zeta_{n_\mathrm{r}})$, and $\rho(b, \zeta_{n_\mathrm{r}}) = -\frac{6.02b+20\log_{10}(1/\zeta_{n_\mathrm{r}})}{10}$ is the inverse of the signal-to-quantization-noise ratio, with its value being a function of quantization bits b and $\zeta_{n_\mathrm{r}} = \frac{\Gamma}{\|y_{n_\mathrm{r}}\|_\infty}$, where $\|y_{n_\mathrm{r}}\|_\infty$ denotes the peak amplitude of y_{n_r} [18]. $\mathbf{n}_q \sim \mathcal{CN}(\mathbf{0}, \mathbf{R}_{\mathbf{n}_q})$ denotes the additive Gaussian quantization noise vector, which is uncorrelated with $\mathbf{y}$, $\mathbf{R}_{\mathbf{n}_\mathrm{q}} = \mathbf{A}(\mathbf{I} - \mathbf{A})\mathrm{diag}(\mathbf{H}(\boldsymbol{\Theta})\mathbf{F}\mathbf{F}^\mathrm{H}\mathbf{H}(\boldsymbol{\Theta})^\mathrm{H} + \sigma^2\mathbf{I})$.

In this paper, we assume that the signal is successfully unfolded by the Modulo ADC when $\hat{\mathbf{k}} = \left\lfloor\frac{\mathbf{y}+\Gamma\mathbf{1}}{2\Gamma}\right\rfloor$, and the recovered signal can be rewritten as

$$\hat{\mathbf{y}} = \mathbf{A}\mathbf{y} + \mathbf{n}_\mathrm{q} = \mathbf{A}\mathbf{H}(\boldsymbol{\Theta})\mathbf{F}\mathbf{s} + \mathbf{e} \tag{7}$$

where $\mathbf{e} = \mathbf{n} + \mathbf{n}_\mathrm{q} \sim \mathcal{CN}(\mathbf{0}, \mathbf{R}_\mathbf{e})$ denotes equivalent noise, $\mathbf{R}_\mathbf{e} = \sigma^2\mathbf{A}^2 + \mathbf{R}_{\mathbf{n}_\mathrm{q}}$. Then, the signal is combined by the combiner $\mathbf{W} \in \mathbb{C}^{N_\mathrm{r}\times N_\mathrm{s}}$ at the Rx can be expressed as

$$\tilde{\mathbf{y}} = \mathbf{W}^\mathrm{H}\hat{\mathbf{y}} = \mathbf{A}\mathbf{W}^\mathrm{H}\mathbf{H}(\boldsymbol{\Theta})\mathbf{F}\mathbf{s} + \hat{\mathbf{e}} \tag{8}$$

where $\hat{\mathbf{e}} = \mathbf{W}^\mathrm{H}\mathbf{e}$. Accordingly, the achievable SE can be expressed as

$$R = \log_2\det(\mathbf{I}_{N_\mathrm{s}} + \mathbf{A}^2\mathbf{R}_{\hat{\mathbf{e}}}^{-1}\mathbf{W}^\mathrm{H}\mathbf{H}(\boldsymbol{\Theta})\mathbf{F}\mathbf{F}^\mathrm{H}\mathbf{H}(\boldsymbol{\Theta})^\mathrm{H}\mathbf{W}) \tag{9}$$

where $\mathbf{R}_{\hat{\mathbf{e}}} = \mathbf{W}^\mathrm{H}\mathbf{R}_\mathbf{e}\mathbf{W}$.

B. Problem Formulation

In this section, we formulated the downlink SE optimization problem of the IRS-aided mmWave MIMO system with Modulo ADCs by jointly designing the Tx and Rx beamformer, and IRS phase shift, which is expressed as

$$\max_{\mathbf{W},\boldsymbol{\Theta},\mathbf{F}} \quad R \tag{10a}$$

$$s.t. \|\mathbf{F}\|_\mathrm{F}^2 \leq P_\mathrm{t}, \tag{10b}$$

$$|\theta_{n_\mathrm{i}}| = 1, n_\mathrm{i} \in \mathcal{N}_\mathrm{i}, \tag{10c}$$

$$b_{n_\mathrm{r}} = b, \forall n_\mathrm{r}, b \in \{2, \ldots, 8\}. \tag{10d}$$

The constraint (10b) limits the transmit power, while (10c) imposes the constant-modulus IRS constraint. (10d) constrains each branch to the same bit resolution. Problem (10) is highly non-convex due to the bilinear coupling among $(\mathbf{W}, \mathbf{F}, \boldsymbol{\Theta})$ and the unit-modulus constraints.

III. Joint Transceiver Beamforming and IRS Phase Shift Design

This section proposes a real-valued genetic algorithm-based scheme to effectively address the joint optimization of the transceiver beamformer and IRS reflection matrix to maximize the SE defined in (10). To the best of our knowledge, this represents the first attempt to employ the proposed scheme to joint transceiver beamformer and IRS phase shifts optimization in multi-variable coupled mmWave MIMO systems. The proposed scheme proceeds through the following steps: 1) initialization of optimization variables and population; 2) specification of the fitness evaluation function; and 3) implementation of selection, crossover, and mutation operations.

A. Initialization of Optimization Variable and Population

First, encode the IRS phase shift matrix as

$$\mathbf{v}^0_{\mathrm{IRS}} = [\arg(\boldsymbol{\theta}^0)] \in \mathbb{C}^{N_\mathrm{i}} \tag{11}$$

The initial population is then generated by perturbing this baseline as follows:

$$\mathbf{V}^p_{\mathrm{tot}} = \mathbf{v}^0_{\mathrm{IRS}} + \mathbf{r}_p \tag{12}$$

where $\mathbf{r}_p, p \in \mathcal{P} = \{1, ..., P_{\text{size}}\}$ is a random Gaussian perturbation vector, and the population size is P_{size}.

B. Specification of the Fitness Evaluation Function

For any optimized individual $\mathbf{V}_{\text{tot}}^p$, the chromosome can be decoded back to $\mathbf{\Theta}^p$, and obtain $\mathbf{H}(\mathbf{\Theta}^p) = \mathbf{H}_{\text{IR}}\mathbf{\Theta}^p\mathbf{H}_{\text{TI}}$. To avoid introducing an additional hyperparameter and bias from initialization, we adopt a noise-only initialization $\mathbf{R}_{\text{e}}^{(0)} = \sigma^2\mathbf{A}^2 \succ 0$, then perform Cholesky and get $\mathbf{R}_{\text{e}}^{(0)} = \mathbf{C}_0\mathbf{C}_0^{\text{H}}$. Then, define the whitened channel as

$$\mathbf{H}_{\text{wh}} = \mathbf{C}_0^{-1}\mathbf{A}\mathbf{H}(\mathbf{\Theta}^p) \tag{13}$$

Then, perform singular value decomposition (SVD) on (13) $\mathbf{H}_{\text{wh}} = \mathbf{U}_{\text{wh}}\mathbf{\Sigma}_{\text{wh}}\mathbf{V}_{\text{wh}}$. The water-filling strategy is adopted to maximize the achievable rate under the power constraint. By applying the Karush–Kuhn–Tucker (KKT) conditions, the optimal power allocation solution is given in closed form as

$$p_{n_{\text{s}}} = [\mu - \frac{1}{\gamma_{n_{\text{s}}}}]^+ \tag{14}$$

where $n_{\text{s}} \in \mathcal{N}_s = \{1, \ldots, N_{\text{s}}\}$, $[x]^+ \triangleq \max(x, 0)$, and μ denotes the water level determined to satisfy the total power constraint $\sum_{n_{\text{s}}=1}^{N_{\text{s}}} p_{n_{\text{s}}} = P_{\text{t}}$. Using the allocated powers, the precoder and the combiner can be formulated as

$$\begin{aligned} \mathbf{W}^p &= \mathbf{C}_0^{-1}\mathbf{U}_{\text{wh}}[:, 1:N_{\text{s}}] \\ \mathbf{F}^p &= \text{diag}(\sqrt{p_1}, \ldots, \sqrt{p_{N_{\text{s}}}})\mathbf{V}_{\text{wh}}[:, 1:N_{\text{s}}] \end{aligned} \tag{15}$$

Then, substituted $\mathbf{\Theta}^p$ and (15) into the fitness function, which can be defined as

$$\text{Fit}^p(\mathbf{F}^p, \mathbf{\Theta}^p, \mathbf{W}^p) = R^p \tag{16}$$

where $R^p = \log_2 \det\left(\mathbf{I}_{N_{\text{s}}} + \mathbf{A}^2\mathbf{H}_{\text{eff}}^p(\mathbf{H}_{\text{eff}}^p)^{\text{H}}\right)$, $\mathbf{H}_{\text{eff}}^p = \mathbf{W}^p\mathbf{H}(\mathbf{\Theta}^p)\mathbf{F}^p$, $\mathbf{R}_{\hat{\mathbf{e}}}^p = (\mathbf{W}^p)^{\text{H}}\mathbf{R}_{\mathbf{e}}^p\mathbf{W}^p$, $\mathbf{R}_{\mathbf{e}}^p = \sigma^2\mathbf{A}^2 + \mathbf{A}(\mathbf{I} - \mathbf{A})\text{diag}(\mathbf{H}(\mathbf{\Theta}^p)\mathbf{F}^p(\mathbf{F}^p)^{\text{H}}\mathbf{H}(\mathbf{\Theta}^p)^{\text{H}} + \sigma^2\mathbf{I})$.

C. Compute Selection, Crossover, and Mutation

We independently draw two parents with uniform probability $\text{a}, \text{b} \sim \mathcal{P}$. Perform arithmetic crossover with probability p_{cros}, and the phase encoding of the offspring can be expressed as

$$\mathbf{V}_{\text{tot}}^{\text{ch}} = \mathbf{V}_{\text{tot}}^{\text{a}} + \boldsymbol{\kappa} \odot (\mathbf{V}_{\text{tot}}^{\text{b}} - \mathbf{V}_{\text{tot}}^{\text{a}}) \tag{17}$$

where $\boldsymbol{\kappa}$ denotes the mixing coefficient vector. $\odot$ denotes the Hadamard product. Apply a Gaussian perturbation to the offspring (17) with mutation probability p_{mut}. Assume the optimal SE of the gth generation is $R_{\max}^g = \max_{(\mathbf{F}^p, \mathbf{\Theta}^p, \mathbf{W}^p)} R^{p,g}$, the minimum iterative algebra $G_{\min}$, and the stagnation threshold ϵ. Allowable continuous stagnation algebra G_{stall}. To preserve the best solutions, an elitism strategy is adopted. In each generation, the best $N_{\text{eli}}, 0 < N_{\text{eli}} < P_{\text{size}}$ individuals are directly copied to the next generation before performing crossover and mutation. Then, the stopping criterion can be designed as

$$\eta^g = R_{\max}^g - R_{\max}^{g-1}, \tag{18a}$$

$$\eta^{g'} \leq \epsilon \cdot \max(1 + |R_{\max}^{g'-1}|), \tag{18b}$$

where $g \geq G_{\min}$, and (18b) holds for all $g' \in \{g - G_{\text{stall}} + 1, \ldots, g\}$. As illustrated in Algorithm 1.

D. Complexity Analysis

In this section, we analyze the complexities of the proposed Algorithm 1 in IRS-aided mmWave MIMO systems with modulo ADC at the receiver front end. The per-individual cost can scale as $\mathcal{O}(N_{\text{t}}N_{\text{i}}N_{\text{r}})$. With population size P_{size} and $G_{\max}$ generations, the overall complexity is $\mathcal{O}(P_{\text{size}}G_{\max}N_{\text{t}}N_{\text{i}}N_{\text{r}})$.

Algorithm 1 The proposed scheme

Input: $P_{\text{size}} = 40$, $G_{\max} = 500$, $p_{\text{cros}} = 0.9$, $p_{\text{mut}} = 0.25$, $G_{\min} = 120$, $G_{\text{stall}} = 30$, $N_{\text{eli}} = 8$, $\epsilon = 10^{-6}$.

Initialize $\mathbf{\Theta}^0$ and encode each individual to $\mathbf{V}_{\text{tot}}^p$, $p \in \mathcal{P}$.
for $g = 1 : G_{\max}$ **do**
  for $p = 1 : P_{\text{size}}$ **do**
    For each p: decode $\mathbf{v}_{\text{tot}}^p$ to $\mathbf{\Theta}_i^p$;
    Perform SVD on (13), water-filling (14), and get $\mathbf{F}^p$ and $\mathbf{W}^p$ based on (15)
    Compute fitness using (16);
    Keep N_{eli} elites;
    Selection based on (17);
    Crossover with p_{c} generating offspring;
    Mutate offspring with p_{m};
  end for
  Update $R_{\max}^g$ and check convergence based on (18).
  If yes, **break**.
end for

Output: Optimized SE.

IV. Simulation Results

We consider a 28 GHz downlink IRS-aided mmWave MIMO system equipped with modulo ADCs at the receiver front end. The Tx transmits at $P_{\text{t}} = 40$ dBm transmit power over $N_{\text{s}} = 4$ data streams, and the noise power is $\sigma^2 = -91$ dB [20]. At the Tx, an 8×8 antenna array. The Rx uses a 4×4 antenna array. An IRS with 16×16 elements assists the communication. The channel follows a sparse multipath model with $L_c = 8$, $c \in \{\text{TI}, \text{IU}\}$ propagation paths. According to the channel model in (2), the pathloss based on distance is denoted as $\text{PL}(d_c)[\text{dB}] = \alpha + 10\beta\log_{10}(d_c) + \xi, \xi \sim \mathcal{N}(0, \sigma_\xi^2)$, where for the LoS component, we set $\alpha = 61.4$, $\beta = 2$, $\sigma_\xi = 5.8$ dB, and for the NLoS component, we set $\alpha = 72.0$, $\beta = 2.92$, $\sigma_\xi = 8.7$ dB [20]. d_{TI} and d_{IU} are randomly selected in the intervals of [50 m, 60 m] and [10 m, 20 m], following a uniform distribution. Unless otherwise specified, the simulation employs this parameter setting. To the best of our knowledge, no prior work evaluates low-resolution or conventional ADCs (full dynamic range and low dynamic range) in the same downlink IRS-aided mmWave MIMO system; therefore, we confine our comparison to our own system, contrasting modulo-ADCs with conventional ADCs.

A. Convergence of the Proposed Optimization scheme

Fig. 3 shows SE versus generation for the proposed scheme, plotting the best in generation $R_{\max}^g$ and population mean $\frac{1}{P_{\text{size}}}\sum_{p=1}^{P_{\text{size}}} R^p$. SE rises rapidly within the first 100 generations, improves more gradually from 100 to 400, and stabilizes

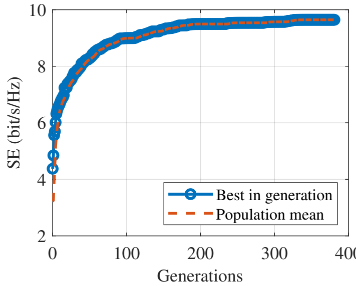

Figure 3. Convergence of the proposed scheme.

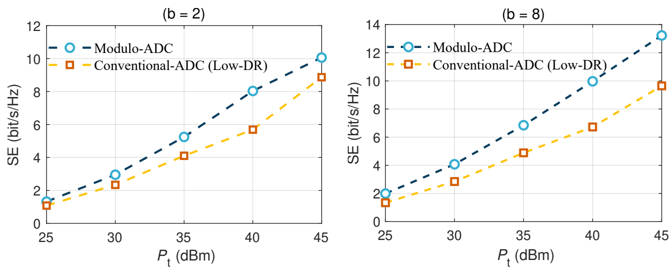

(a) (b)

Figure 4. Comparison of the SE of modulo and conventional ADCs in the low dynamic range setting, where both thresholds are set to $1/3$ of the input peak ($\zeta_{n_\mathrm{r}} = 0.33$). The transmit power P_t ranges from 25 to 45 dBm in 5 dB steps. **(a)** $b = 2$. **(b)** $b = 8$.

near generation 400 at 9.75 bit/s/Hz. The initial about 1.2 bit/s/Hz gap (Population mean is less than Best in generation) evidences exploration with standout elites; its collapse to no indicates population-wide convergence and toward a near-optimal solution.

B. Spectral Efficiency Evaluation

1) Modulo ADC vs. Low DR ADC: We first consider the low dynamic range case, where both the conventional and modulo ADCs use the same threshold, set to $1/3$ of the input peak ($\zeta_{n_\mathrm{r}} = 0.33$). The conventional ADC suffers from clipping distortion, while the modulo ADC folds the samples into $[-\Gamma, \Gamma)$ and employs the HoD algorithm for recovery [14]. The HoD recovery uses order $N_{\mathrm{ord}} = 2$ with a sampling rate of $6.67 f_{\mathrm{Nyq}}$. According to Fig. 4a and Fig. 4b, modulo ADCs consistently achieve higher SE than conventional ADCs under the same bit resolution and transmit power, with the advantage most pronounced at low resolution and high P_t (e.g., $b = 2$, $P_\mathrm{t} = 45$ dBm: 11.67 vs. 9.64 bit/s/Hz). Increasing b further enhances the modulo ADC (e.g., $b = 8$, $P_\mathrm{t} = 45$ dBm: 13.22 vs. 9.64 bit/s/Hz), whereas the SE of the conventional low-DR ADC saturates due to clipping, showing that even mild clipping can significantly degrade system SE.

2) Modulo ADC vs. Full DR ADC: In Fig. 5, we compare the SE of modulo and full-DR conventional ADCs. Modulo ADCs consistently achieve higher SE under the same resolution, with the advantage most pronounced at low b and high P_t (e.g., $b = 2$, $P_\mathrm{t} = 45$ dBm: 13.24 vs. 12.11 bit/s/Hz). At $b = 8$, the conventional ADC finally matches the modulo ADC. This highlights that even without clipping, conventional ADCs require higher resolution to reach the same SE, whereas modulo ADCs achieve the target SE with fewer bits.

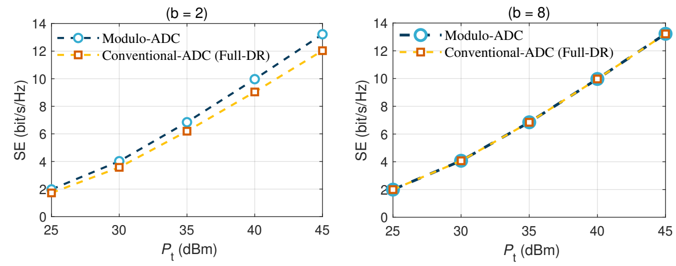

(a) (b)

Figure 5. Comparison of SE between modulo and full-DR conventional ADCs. The full-DR ADC sets its threshold equal to the input peak, while the modulo ADC uses $1/50$ of the input peak ($\zeta_{n_\mathrm{r}} = 0.02$). The transmit power P_t ranges from 25 to 45 dBm in 5 dB steps. **(a)** $b = 2$. **(b)** $b = 8$.

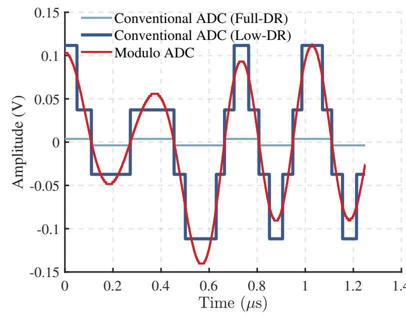

Figure 6. Comparison of ADC schemes with 2-bit resolution. The classical ADC (full DR) sets its threshold to the signal peak, avoiding clipping. Both the low-DR ADC and the modulo ADC use a reduced threshold equal to $1/30$ of the peak ($\zeta_{n_\mathrm{r}} = 0.03$).

Discussion. To gain further insight, we examine how different ADCs affect the waveform. Fig. 6 shows the time-domain outputs of a 16-QAM signal at 2-bit resolution. The full-DR ADC avoids clipping by setting its threshold to the signal peak, but requires higher dynamic range and cost. The low-DR ADC applies a reduced threshold ($1/30$ of the peak), leading to severe distortion. The modulo ADC also uses the reduced threshold but folds samples within the threshold range, preserving information for subsequent digital recovery. This confirms that modulo ADCs sustain fidelity under stringent bit and threshold constraints, whereas conventional ADCs either distort the signal or demand higher resolution.

C. Bit-Error Rate Evaluation

In this section, we begin by examining the received constellation diagrams to illustrate the effect of quantization. Fig. 7 compares constellation recovery for a modulo ADC and a full-DR conventional ADC at 2-bit resolution. The modulo ADC produces scatter points that are tightly clustered around the ideal constellation locations, whereas the full-DR conventional ADC exhibits a markedly more dispersed distribution.

To quantify this observation, we next evaluate the BER, defined as

$$\mathrm{BER} = \frac{1}{N_b} \sum_{i=1}^{N_b} \mathbf{1}\{b_i \neq \hat{b}_i\},$$

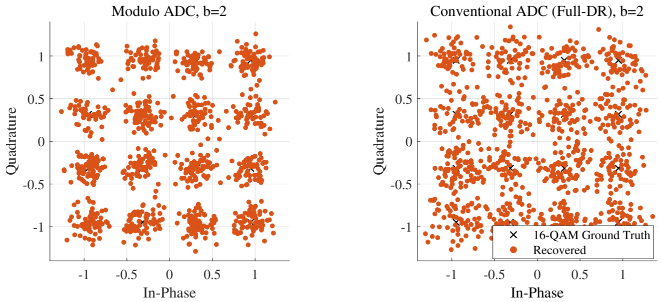

Figure 7. Constellation diagrams of modulo ADC and classical full-DR ADC with $b = 2$ for 16-QAM input.

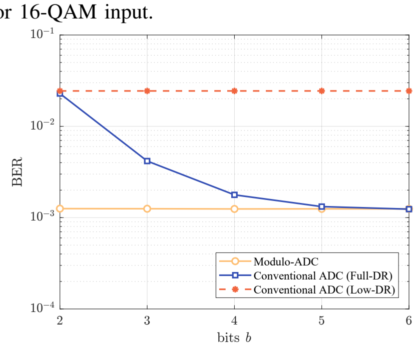

Figure 8. BER vs. ADC resolution $b \in [2, 6]$.

where N_b is the total number of transmitted bits, $b_i \in 0, 1$ denotes the i-th transmitted bit, $\hat{b}_i$ is the corresponding detected bit, and $\mathbf{1}\{\cdot\}$ is the indicator function.

We evaluate three ADC schemes: **1)** a modulo ADC with threshold set to $1/50$ of the input peak ($\zeta_{n_r} = 0.02$), **2)** a low-DR conventional ADC with the same threshold as the modulo ADC, and **3)** a full-DR conventional ADC. Their BER performance as a function of quantization bit depth b is shown in Fig. 8, with $N_b = 40000$ transmitted bits per curve. The modulo ADC maintains a nearly constant BER of 1.25×10^{-3} across the tested range. The full-DR ADC exhibits monotonically decreasing BER with increasing b, reaching parity with the modulo ADC at $b = 6$. In contrast, the low-DR ADC remains around 2.44×10^{-2}, indicating clipping-dominated performance.

V. Conclusion

This work addresses two practical limiting factors of the mmWave MIMO system, namely propagation blockage and ADC saturation, by studying an IRS-aided downlink architecture equipped with a modulo ADC receiver front end and an explicit receiver-side quantization model. We formulate SE maximization under a total transmit power budget, modulus IRS constraints, and bit resolution constraints, and devise an efficient algorithm that jointly optimizes the transceiver beamforming and IRS reflection matrix. Experimental results confirm that the modulo ADC consistently outperforms conventional ADCs by delivering higher SE and lower BER with fewer quantization bits, while effectively mitigating saturation-induced clipping.

References

[1] M. Xiao, S. Mumtaz, Y. Huang, L. Dai, Y. Li, M. Matthaiou, G. K. Karagiannidis, E. Björnson, K. Yang, I. Chih-Lin, *et al.*, "Millimeter Wave Communications for Future Mobile Networks (Guest Editorial), Part I," *IEEE J. Sel. Areas Commun.*, vol. 35, pp. 1425–1431, July 2017.

[2] R. W. Heath, N. Gonzalez-Prelcic, S. Rangan, W. Roh, and A. M. Sayeed, "An Overview of Signal Processing Techniques for Millimeter Wave MIMO Systems," *IEEE J. Sel. Topics Signal Process.*, vol. 10, pp. 436–453, Apr. 2016.

[3] M. Di Renzo, A. Zappone, M. Debbah, M.-S. Alouini, C. Yuen, J. De Rosny, S. Tretyakov, *et al.*, "Smart Radio Environments Empowered by Reconfigurable Intelligent Surfaces: How It Works, State of Research, And The Road Ahead," *IEEE J. Sel. Areas Commun.*, vol. 38, pp. 2450–2525, Nov. 2020.

[4] C. Pan, H. Ren, K. Wang, W. Xu, M. Elkashlan, A. Nallanathan, and L. Hanzo, "Multicell MIMO Communications Relying on Intelligent Reflecting Surfaces," *IEEE Trans. Wireless Commun.*, vol. 19, pp. 5218–5233, Aug. 2020.

[5] E. G. Larsson, O. Edfors, F. Tufvesson, and T. L. Marzetta, "Massive MIMO for Next Generation Wireless Systems," *IEEE Commun. Mag.*, vol. 52, pp. 186–195, Feb. 2014.

[6] K. Zhi, C. Pan, H. Ren, and K. Wang, "Uplink Achievable Rate of Intelligent Reflecting Surface-Aided Millimeter-Wave Communications with Low-Resolution ADC And Phase Noise," *IEEE Wireless Commun. Lett.*, vol. 10, pp. 654–658, Mar. 2021.

[7] J. Li, R. Wang, and E. Liu, "Passive Beamforming Design for IRS Communication System with Few-Bit ADCs," in *2021 4th International Conference on Information Communication and Signal Processing (ICICSP)*, (Shanghai, China), pp. 501–505, Sept. 2021.

[8] J. Chen, W. Tan, T. Liu, S. Li, Y. Li, and M. Zhou, "Spectral Efficiency for IRS-assisted Uplink mmWave Massive MISO Systems with Low-Resolution ADCs," *Phys. Commun.*, vol. 55, p. 101865, Dec. 2022.

[9] Y. Wang, X. Chen, Y. Cai, and L. Hanzo, "RIS-aided Hybrid Massive MIMO Systems Relying on Adaptive-Resolution ADCs: Robust Beamforming Design And Resource Allocation," *IEEE Trans. Veh. Technol.*, vol. 71, pp. 3281–3286, Mar. 2022.

[10] X. Chen, H. Ren, C. Pan, Z. Peng, K. Zhi, Y. Liu, X. Xi, A. Garcia Armada, and C.-X. Wang, "Performance Analysis on RIS-aided Wideband Massive MIMO OFDM Systems with Low-Resolution ADCs," *IEEE Trans. Wireless Commun.*, vol. 24, pp. 10227–10243, Dec. 2025.

[11] M. Ma, N. Thanh Nguyen, I. Atzeni, and M. Juntti, "Joint Beamforming Design And Bit Allocation in Massive MIMO with Resolution-Adaptive ADCs," *IEEE Trans. Wireless Commun.*, vol. 24, pp. 8711–8726, Oct. 2025.

[12] Y. Liang, L. Zhao, and Q. Tang, "Design of High Dynamic AGC Control Model And Signal Processing Algorithm for Software Radio Receivers," in *2020 IEEE 9th Joint International Information Technology and Artificial Intelligence Conference (ITAIC)*, vol. 9, (Chongqing, China), pp. 1442–1446, 2020.

[13] J. Wu, G. Lin, L. Ruan, and T. Liu, "System Design of A Class-D Audio Power Amplifier Circuit with High-Precision AGC Control," in *2024 4th International Conference on Communication Technology and Information Technology (ICCTIT)*, (Guangzhou, China), pp. 251–254, 2024.

[14] A. Bhandari, F. Krahmer, and R. Raskar, "On Unlimited Sampling And Reconstruction," *IEEE Trans. Signal Process.*, vol. 69, pp. 3827–3839, Dec. 2021.

[15] L. Gan and H. Liu, "High Dynamic Range Sensing using Multi-Channel Modulo Samplers," in *2020 IEEE 11th Sensor Array and Multichannel Signal Processing Workshop (SAM)*, (Hangzhou, China), pp. 1–5, 2020.

[16] Y. Gong, L. Gan, and H. Liu, "Multi-Channel Modulo Samplers Constructed from Gaussian Integers," *IEEE Signal Process. Lett.*, vol. 28, pp. 1828–1832, Aug. 2021.

[17] W. Yan, L. Gan, S. Hu, and H. Liu, "Towards Optimized Multi-Channel Modulo-ADCs: Moduli Selection Strategies And Bit Depth Analysis," in *Proc. IEEE Int. Conf. Acoust., Speech Signal Process. (ICASSP)*, (Seoul, South Korea), pp. 9496–9500, IEEE, Apr. 2024.

[18] Z. Liu, A. Bhandari, and B. Clerckx, "λ–MIMO: Massive MIMO via Modulo Sampling," *IEEE Trans. Commun.*, vol. 71, pp. 6301–6315, Nov. 2023.

[19] Q. Wu, S. Zhang, B. Zheng, C. You, and R. Zhang, "Intelligent Reflecting Surface-Aided Wireless Communications: A Tutorial," *IEEE Trans. Commun.*, vol. 69, pp. 3313–3351, May 2021.

[20] M. R. Akdeniz, Y. Liu, M. K. Samimi, S. Sun, S. Rangan, T. S. Rappaport, and E. Erkip, "Millimeter Wave Channel Modeling And Cellular Capacity Evaluation," *IEEE J. Sel. Areas Commun.*, vol. 32, pp. 1164–1179, June 2014.